SAND2000-1797J

Thermal Stability of Photosensitive Bragg Gratings in Sputter-Deposited Germanosilicate Glass

by

B.G. Potter, Jr.*, K. Simmons-Potter, and T.D. Dunbar
Sandia National Laboratories
Albuquerque, NM 87185

Abstract

The thermal stability of photo-imprinted Bragg gratings formed in reactive-atmosphere, RF-magnetron sputtered germanosilicate thin films was evaluated in terms of point defect modifications observed during isochronal annealing. Optical and magnetic spectroscopies were utilized to evaluate structural relaxation in these sputtered glasses on both a local and medium-range size scale. Depending upon the substrate temperature used during deposition, significant structural rearrangement was found to occur with increasing post-deposition anneal temperature to 600 C. This resulted in changes in the photobleaching response of the material itself as the identity of optically active structural defects evolved. Based on a color center model for photosensitivity in these materials and measured changes in optical absorption with annealing, the thermal stability of a photo-imprinted Bragg grating was modeled. Good qualitative agreement with experiment was observed.

*corresponding author: SNL, Dept. 1846, MS 1405; e-mail: bgpotte@sandia.gov; voice: 505-844-9919; fax: 505-844-2974.

1. Introduction

The opportunity for low-loss, in-fiber manipulation of optical signals and the realization of physically robust, remote optical sensing elements have been major motivating factors in the development and application of optical-fiber-based, photosensitive Bragg gratings. The production of reliable devices with predicable behavior has been enabled by the development of a fundamental understanding of the underlying interaction between the glass and the optical radiation used to photo-imprint these refractive index structures. In fibers, such knowledge has been used to both optimize the photosensitive response of the material and to understand issues regarding the environmental stability of the resulting Bragg gratings [1,2].

Our recent efforts have focused on the migration of this photosensitive materials technology to a planar format, thus enabling fundamentally new devices and operational modes compatible with high density, integrated photonic architectures and fabrication requirements [3]. Based on an established link between oxygen-deficient centers associated with Ge in GeO_2-doped silica glass and the photosensitive response, we have pioneered the use of reactive-atmosphere, RF-sputtering as a means to synthesize highly photosensitive germanosilicate glass films without the need for post-deposition treatment of the material [4-6]. Moreover, through control of deposition parameters, we have demonstrated *in-situ* control of the magnitude, sign, and dispersion of the photo-induced refractive index change observed through direct modification of the underlying precursor defects participating in the photosensitive process [6,7]. These efforts have shown that the primary photosensitive mechanism operating in our materials under the exposure conditions used is consistent with the color center model, i.e. the refractive index changes

DISCLAIMER

observed result directly from the photo-induced modification of the absorption function for the material through the Kramers-Kronig relationship [7].

While the compositional make-up of both fiber and thin film-based materials are similar, our research has highlighted the dramatic influence of processing on material defect structure and its effect on optical performance [3,6]. Beyond the need for enhanced photosensitivity, it is of interest also to investigate the stability of these alternative photosensitive defect structures and the consequent impact on the environmental response of photo-imprinted devices, e.g. thermal and ionizing radiation resistance. Since the optical behavior of defect structures present in the glass is the primary contributor to a photo-induced refractive index change, any subsequent modification of the defect structure (through thermal means or otherwise) will significantly impact the condition of a given photo-imprinted device structure and, hence, its operational characteristics. An understanding of the interdependence of defect structure modification and device-level response is critical to the reliable application of photosensitive structures under a variety of conditions.

In the present work, we will examine the impact of elevated temperature on reactive atmosphere, RF-magnetron sputtered germanosilicate thin films. Investigations to probe both the local and medium-range structure, the corresponding effect on the material optical behavior and the effects on the performance of Bragg gratings photoimprinted into these glasses will be discussed. Knowledge of material-level effects will provide a first-order approach to predicting the thermal stability of these devices.

2. Experimental

Germanosilicate films (2 micron thickness) were deposited onto fused silica substrates using reactive atmosphere, RF-magnetron sputtering. In this approach, a Si/Ge alloy (50:50 mol%) was sputtered under an oxygen atmosphere to produce the oxide glass films. A complete discussion of the sputtering conditions can be found in References 4 and 8. We have shown that control of the oxygen partial pressure and the substrate temperature during sputtering can be used to tailor the population and characteristics of the oxygen-deficient point defects present in the final film [8]. The present work will describe investigations of films deposited to substrates held at 180 C and 600 C, termed LT and HT, respectively.

Thin film atomic structure was probed using both optical and magnetic spectroscopies to evaluate the impact of processing conditions, UV-irradiation and thermal annealing on both the local and medium-range film structure. Absorption spectroscopy (PE Lambda 900, dual-beam spectrophotometer) was coupled with electron paramagnetic resonance (EPR) to gain insight into the behavior of optically active point defects in the films.

Photosensitive film samples taken from a single substrate were used for comparative spectroscopic studies. Optical absorption samples were approximately 1 cm in width and 2 cm in length. This allowed for excellent signal/noise in the measurement as there was no beam clipping. Samples were also examined using unpolarized, waveguide Raman spectroscopy to provide additional evidence for structural modification after thermal annealing.

Room temperature X-band EPR was performed using a Bruker EMX spectrometer. Samples for the EPR measurements were sliced into segments approximately 1 cm long by 2-3 mm wide. Three such segments each were inserted into a 4 mm inner-diameter quartz tube which was then placed in the microwave cavity for the spin-resonance studies. With this sample loading, no degradation in the Q of the cavity was observed. The following spectral conditions were employed for quantitative comparison of Ge E' signals: microwave power, 0.2 mW; modulation amplitude, 2.5 G; conversion time, 82 ms; and time constant, 655 ms. When defect signals did not overlap, the observed signal was doubly integrated and compared to weak pitch. Often, however, Si E' signals overlapped with the Ge E' $g_{||}$. In these cases, the intensity of the Ge E' $g_{\perp}$ was compared to a SiO_2:GeO_2 sample spectrum in which the Ge E' signal was so strong that no detectable Si E' signal was present. The relative amount of Ge E' could then be compared to weak pitch. From multiple observations of the same weak pitch sample over the course of the experiment, we estimate a relative error of 3% in our ability to compare the same sample to itself. An absolute error in the ability of the EPR spectrometer to count Ge E' centers based upon the above-mentioned comparison to weak pitch was not attempted. We estimate that our minimum detection limit is 2×10^{15} Ge E' per cm^3.

UV-irradiation of the samples was performed using a KrF excimer laser (Lambda-Physik) operating at 248 nm with 15 mJ/cm^2/pulse at a 15 Hz repetition rate. The typical total fluence used to fully saturate the absorption change in these materials was 15 kJ/cm^2. As-deposited and UV-irradiated films were subjected to isochronal anneals ranging from 100 C to 700 C for 15 minute soak times under flowing He (99.999%). Optical and EPR data were obtained at room temperature after each treatment step. As

previously stated, optical and magnetic spectroscopic analyses were performed on samples cut from the same substrate. The optical and EPR samples were heat-treated together.

In addition to an examination of the glass itself, the thermal stability of a photo-imprinted Bragg grating was investigated. Bragg gratings were written using a phase mask patterning approach with the same excimer laser conditions as those used for the material study [7]. A total fluence of approximately 15 kJ/cm^2 was again used to insure a saturated refractive index change in the glass. For grating thermal stability studies, the device was probed normal to the film plane at a wavelength of 632.8 nm (3 mW, HeNe) after each step of the isochronal anneal schedule given above. Again, optical measurements were performed at room temperature. The intensity of the 1st order diffracted beam was monitored at a Si photodiode using lock-in detection techniques. Standardized mounting of the thin film allowed reproducible sampling of the same region of the film after each isochronal anneal step. Experimental error in the measurement of diffracted beam intensity is estimated to be $\pm$ 3%.

3. Results

3.1 Optical

Figures 1a and 1b contain representative optical absorption spectra for glass films deposited to 180 C (LT) and 600 C (HT) fused silica substrates both in the as-deposited state and after a saturating UV-exposure, respectively. Evident is a significant difference in the UV-response between the two materials; the LT sample exhibits a broad-band bleach in the UV portion of the absorption spectrum that contrasts the simultaneous band

growth (at approximately 200 nm) and bleach (at 240 nm) that is observed in the HT spectrum. Differences in the effect of thermal annealing on the optical absorption of previously UV-exposed films are also observed. Figures 2 (a) and (b) depict representative absorption spectra for LT and HT glasses respectively that have been UV bleached and then, subsequently, subjected to a thermal anneal sequence. The growth and decay of optical absorption features as a function of isochronal anneal temperature is summarized in Figures 3 and 4 for the LT and HT films. Figures 3(a) and 4(a) depict the anneal dynamics for the as-deposited films while Figures 3(b) and 4(b) present data for the UV irradiated films. In the latter figures, data are given for the relevant absorption features for the films as-deposited and then following UV irradiation and thermal anneal and, finally for the LT film, following a second UV exposure and anneal sequence. Values for absorbance (or optical density) at wavelengths of 200 nm and 240 nm are reported in the figures as these wavelengths correspond to absorption features commonly associated with known oxygen-deficient Ge defect centers [9-12]. In general, the broad-band nature of the UV absorption typically exhibited in the sputtered films precludes the use of curve-fitting to extract an integrated intensity for these features. The use of single-wavelength optical density, therefore, represents a first-order approach to track general trends in optical absorption with UV-irradiation and heat treatment.

Figure 3 shows significant growth in the absorption bands following anneal in both the as-deposited LT and the UV-exposed LT films, up to temperatures of approximately 400 C. At anneal temperatures above 400 C all bands begin to decay. After the initial isochronal anneal sequence, the LT-glass shows an apparent change in its response to UV (Figure 3(b)), showing some growth in the 200 nm absorption and

significant bleaching of the 240 nm absorption. This is in direct contrast to the broad-band bleaching observed in the as-deposited state. Evidence for the change in UV response following the first set of anneals can be seen in another form in Figure 5 which contains representative absorption spectra for the LT material showing UV effects on the absorption spectrum both before and after annealing. The as-deposited HT film in Figure 4(a) shows little effect of annealing to 450 C, however the UV exposed film (Figure 4(b)) exhibits decay of the 200 nm absorbance and growth of the 240 nm absorbance with increasing anneal temperature. In this latter case, the anneal sequence tends to counter the relative band modifications resulting from UV exposure of the material (see Figures 1(b) and 2(b)). A comparison of the band behavior in Figures 3b and 4b following the second UV exposure shows that the annealed then re-irradiated LT films display identical trends in the second anneal sequence to that observed in the HT material with an absorbance decay at 200 nm and continuing growth of the 240 nm band.

Figure 6 depicts a series of waveguide Raman spectra for LT and HT materials before and after a 465 C, 30 minute thermal treatment under flowing He. While there is limited change in the HT-glass vibrational behavior after thermal annealing, the LT spectrum shows the disappearance of a vibrational mode at 780 cm-1, associated with the presence of non-bridging oxygen bonds [13], and a decrease in vibrational energy of the symmetric stretching band at 410 cm-1. This latter feature is associated with Si-O-Si, Si-O-Ge, Ge-O-Ge linkages [14,15]. Again, the two glasses exhibit significant differences in their thermal response, this time evidenced at a medium-range structural scale. There was no measurable change in the Raman characteristics of either the LT or HT-type materials after UV-exposure.

3.2 EPR

Further evidence for unique defect dynamics resulting from UV exposure of both the LT and HT films are found in the EPR data of Figures 7 and 8. These Figures depict EPR spectra obtained from LT and HT samples, respectively, before and after a saturating UV-exposure. Analogous to the absorption findings, the two glasses exhibit distinct differences in the unpaired spin response with UV-irradiation. The LT films (Figure 7) show a 36 % decrease in spin density of unpaired spin centers associated with the presence of approximately axially symmetric Ge E' centers, at $g_{\perp} = 1.9943$ and $g_{\parallel} = 2.0010$ with an uncertainty of ±0.0002. Spin density values for the LT films go from 4.2 x 10^{16} spins/cm^3 to 2.7 x 10^{16} spins/cm^3 following UV exposure. In contrast, the HT samples (Figure 7) initially exhibit a resonance intensity of approximately 1.2 x 10^{17} spins/cm^3 in the same g-range. This spin density increases to 1.3 x 10^{19} spins/cm^3 after UV exposure.

The effect of isochronal annealing on both materials, however, tends to decrease the unpaired spin resonance observed as shown in Figures 9 and 10 which summarize the EPR spin density results. This thermally induced decrease in spin density associated with oxygen deficient Ge sites in the glass is, in fact, observed in both as-deposited and UV-exposed materials. Of particular interest is a reversal in the effect of UV-irradiation again evidenced in the LT-type glass after isochronal annealing to 600 C. After annealing, the material now exhibits a very large increase in unpaired spin density upon UV exposure (Figure 9b), from a value below that of noise (~2 x 10^{15}) to a value of 4.1 x 10^{18} spins/cm^3. The corresponding EPR spectra before and after the second UV-

exposure are presented in Figure 11. Focusing on the EPR spectral data of Figures 7 and 11, it is clear the post-anneal UV-response exhibited in the LT material is in direct contrast to the UV-response of the material in its as-deposited condition. However, this response coincides well with the post-anneal differences in the optical absorption response discussed above and shown in Figure 5.

3.3 Bragg Grating Thermal Stability

The observed diffracted intensities from Bragg gratings photo-imprinted into both LT and HT glasses are depicted in Figure 12 as a function of isochronal anneal temperature. Again, the effect of the different substrate temperatures used during material synthesis can be observed, this time in the thermal stability of the grating structure. It is clear that the two gratings exhibit very different responses to the annealing schedule; the LT samples show an initial decrease in grating contrast while the HT diffraction intensity actually increases between room temperature and 300 C. The HT gratings maintain a more presistent 1st order diffracted intensity throughout the entire temperature range of the study with both materials showing marked decreases in the diffraction intensity beyond 600 C. Interestingly, despite the changes in absorption and EPR behavior indicated in the LT materials studies above in the 200 – 400 C annealing range, these samples still exhibit significant diffraction intensity (>50 % of the original intensity) even up to 600 C.

4. Discussion

4.1 Material Behavior

The distinct responses exhibited by the LT and HT glass films to UV-irradiation have been examined in detail in previous work [5-7] in which they were explained by the presence of varied precursor point defect structures in the glass. Charge injection and UV-irradiation studies coupled with optical absorption, EPR and dielectric analysis indicated that the primary precursor defect in the HT materials is a neutral, oxygen-deficient Ge site, most likely a neutral oxygen monovacancy (NOMV) [5]. This state exhibits an absorption band at around 240 nm and is converted to a Ge E' center (absorption at 200 nm) upon 248 nm irradiation. In contrast, at least one LT material precursor state is a neutral, isolated dangling bond state associated with Ge that is converted to a charged, diamagnetic species under UV-irradiation [5].

From a technological standpoint, the unique bleaching behaviors associated with these defect states can allow us to tailor the photosensitive response of our materials. As a result, we have been able to demonstrate control of the magnitude and sign for Δn through synthesis control. The broad-band UV-bleach characteristics of the LT sample, for example, have been used to achieve very high, UV-induced, negative refractive index changes (-5 x 10-3) without the need for post-deposition, reducing atmosphere, thermal processing [8]. The main issue under investigation in the present study is the impact of these alternative defect structures on the thermal stability of the material optical behavior and the corresponding performance of a photo-imprinted grating.

From the data presented in the last section, it is clear that thermal annealing causes significant changes in both the local and medium-range structure of the glass films

as evidenced through both optical and magnetic spectroscopic probes. These structural modifications are quite pronounced in the low substrate temperature glass (LT-type). Optical absorption indicates that, not only is the optical density altered after thermal treatment, but the spectral distribution of absorption strength is also changed in this material (see Figures 2,3). Both as-deposited and UV-bleached LT samples exhibit the formation and sharpening of absorption features at approximately 240 nm and 200 nm, peaking in absorption strength at an isochronal anneal temperature of 400 C. This behavior is accompanied by a decrease in the spin density of isolated, dangling bond defects associated with oxygen-deficient Ge (Figure 7) that is reduced to below the detection threshold for the EPR by 200 C. These results indicate that the defect structure of the glass has been transformed from that containing EPR-active isolated Ge dangling bond states with other, as yet unidentified, diamagnetic centers, to that containing a more commonly observed collection of neutral oxygen vacancies (absorption around 240 nm [9,11,12]) and conventional, Ge E' centers (absorption at 200 nm [12,16-17]).

These structural modifications have a dramatic impact on the UV-response of the material as observed in Figure 5. Here, the influence of UV-irradiation on the absorption spectrum of a LT glass is shown both in an as-deposited state and after isochronal annealing to 600 C. Immediately evident is a change in the bleaching response; the as-deposited material exhibits the broad-band bleach characteristic of the LT glasses (e.g. Figure 1) while after annealing, the bleach response most closely resembles that of the HT glass. The EPR response (Figure 11) also indicates a thermally induced transition in bleach behavior in which UV-irradiation actually produces an increased Ge spin density in the previously annealed LT glass. In the as-deposited state, the same material showed

a decreased spin density with UV-exposure. The EPR data further reveal that the thermal stability of the isolated Ge-dangling-bond states that exist in the as-deposited LT material is demonstrably different than that observed for the UV-induced Ge E' centers formed in the thermally annealed glass (see Figure 9). This observation also lends support to previous work [5] that identified the neutral, oxygen-deficient, Ge-dangling-bond state as the precursor defect responsible for the initially high EPR signal in the as-deposited LT material. While this state and the Ge E' center occur at very similar EPR g-values, they are not the same structural entity as evidenced by UV and charge injection effects [5] and now thermal stability.

The LT glass Raman data complements the local structural insight obtained from the absorption and EPR studies. Here, the disappearance of the non-bridging oxygen band (at 780 cm^{-1}) after heat-treatment is interpreted in terms of an increased degree of crosslinking within the glass network. In the as-deposited LT material, the symmetric stretching band for the bridging oxygen bond is found at a higher energy (410 cm^{-1}) than that exhibited in melt-derived materials [14]. This indicates the presence of strained or distorted bonds that can alter the bridging bond angles participating in that vibration. Such effects have been observed under applied stresses in bulk germania and silica glass [18,19]. After heat-treatment, however, this band shifts to lower energies that are consistent with annealed, bulk glass [14]. Based on these data, it is apparent that the LT glass is undergoing structural rearrangement during the thermal annealing. This is not a surprising result; under the deposition conditions used, newly deposited atomic species would not have had sufficient thermal energy to permit rearrangement to more energetically stable configurations, thus favoring the formation of structures which depart

from those of a fully annealed glass. The isochronal treatments provide the thermal energy necessary to allow structural relaxation, thus enabling the development of local and medium range structural characteristics more representative of a melt-derived glass.

The trends with heat-treatment observed in HT-type glass films were more subtle; these materials exhibit optical absorption and vibrational characteristics more consistent with an annealed glass structure in their as-deposited state due to the higher substrate temperature used during deposition. The HT films exhibit more distinct absorption features at 200 and 240 nm than observed in the LT material (Figure 1). This is accompanied by Raman spectra more closely resembling that of the annealed LT material or bulk glass of similar composition (Figure 6).

With isochronal annealing, the as-deposited, HT films show some sharpening of both 200 and 240 nm absorption bands with the 200 nm band reaching at peak in intensity between 300 and 350 C (Figures 2b, 4a) . This is again indicative of structural rearrangement at a local scale which most likely narrows the range of defect conformations present and, hence, the degree of inhomogeneous broadening contributing to the absorption spectrum. The EPR analysis of this glass also shows a monotonic reduction in the unpaired spin density of approximately 2 orders of magnitude with increasing temperature to 450 C (Figure 10). Minimal shifts to lower energy in the symmetric stretching 410 cm-1 Raman band were observed after thermal annealing as well (Figure 6). The as-deposited, HT Raman spectrum does not show the non-bridging oxygen vibrational band that was evidenced in the LT sample, indicating that the HT material started out with a greater degree of network connectivity than the LT material.

In UV-bleached, HT glass, the predominant effect of the isochronal anneal is to reverse UV-induced changes in the absorption spectrum. With increasing temperature, the absorption strength at 200 nm and 240 nm decreases and increases, respectively, recovering to near their as-deposited values by 350 C (see Figure 4b). At still higher anneal temperatures, these trends continue resulting in final optical densities at 200 and 240 nm that are lower and higher than their as-deposited values, respectively. The Ge E' EPR spectrum mirrors the general trend for the 200 nm optical density. A gradual decrease in the Ge E' center spin density from greater than 1 x 10^{19} Ge E' per cm^3 after UV-bleaching to below the detection threshold (<2 x 10^{15} Ge E' per cm^3) at 450 C is observed (Figure 10). These trends can be interpreted in terms of the thermally induced liberation of charge that was trapped after the ionization of neutral oxygen vacancies during UV-irradiation. As this charge is freed to recombine with Ge E' centers, their population decreases (seen in EPR and 200 nm absorption band reduction) and the population of neutral oxygen vacancies increases (observed in the increasing 240 nm absorption). This process most likely occurs simultaneously with some limited structural relaxation that ultimately results in the formation of more well-defined absorption bands and shifts in the vibration bands observed in Raman associated with a reduction in the number of strained bonds in the material.

Overall, the structural evidence gathered during the isochronal anneals of the HT and LT glass corroborates differences in the previously observed UV-response of these sputtered materials, i.e. that there are distinct differences in the local and medium range structure in materials synthesized using ambient and elevated substrate temperatures.

These differences in structure can be directly tied to the substrate temperature used during deposition and the associated degree of rearrangement allowed during deposition.

4.2 Bragg Grating Thermal Stability

The established dependence of the glass photosensitive response on atomic structure, combined with the distinct thermal responses exhibited by the two glass types of the present study, indicates that there should be substantial differences in the thermal stability exhibited by photo-imprinted Bragg gratings in each material. This was indeed observed (see Figure 12). Given the large changes in the local and medium range structure for the LT-type glass that was observed in the magnetic and optical spectroscopy data, it was somewhat surprising to observe significant diffraction intensity from the LT-Bragg grating, even to annealing temperatures in excess of 400 C where EPR, absorption, and Raman spectroscopies all indicate the occurrence of structural relaxation.

The spectroscopic data for the LT material indicate that the defect structures participating in a photosensitive response are altered during these anneal treatments, resulting in changes to the absorption spectrum of the glass and an associated change in the refractive index (through the Kramers-Kronig relationship). It is anticipated that such a thermally induced refractive index change should alter the photo-induced grating index contrast (i.e. the peak-to-valley difference in refractive index along the grating length) that directly determines the grating diffraction efficiency.

Further insight into the mechanisms responsible for the observed grating response was gained through modeling the diffraction efficiency of a Bragg grating in these

materials as a function of annealing temperature. A hypothetical grating was considered in which the extreme index regions of the grating pattern were taken to correspond to the as-deposited and UV-exposed glass (see Figure 13). Variations in the peak-to-valley refractive index modulation along the grating can then be approximated using the thermally induced changes in refractive index of as-deposited and UV-exposed material calculated using experimental absorption data and the Kramers-Kronig relationship. These calculated index changes were then used to estimate the thermally induced modification of the initial, UV-imprinted peak-to-valley index modulation (grating contrast). The anticipated 1st order diffracted intensity for a sinusoidal phase grating was then calculated using the equation below in which l is the beam diameter, z is the observation distance and m is the peak phase delay for a grating with line spacing, d, i.e. $(\Delta n)d\sin\theta$:

$$I_{peak} = \left(\frac{l^2}{\lambda z}\right)^2 \left(\frac{m^2}{16}\right) \qquad (1)$$

Figures 14 and 15 contain comparisons of modeled and experimental normalized diffracted intensities for photosensitive gratings in the LT and HT glasses, respectively. While there are discrepancies between the model and experiment in both cases, in the HT films these are slight. In the LT glass (Figure 14) the model underestimates the observed diffraction intensity in the 150 to 250 C range. However, the retention of significant diffraction intensity (and, hence, grating contrast) is correctly predicted out to 450 C, beyond the temperature range in which the material undergoes significant structural

rearrangement. The model more closely predicts the experimental data for the HT glass (Figure 15). Even the enhancement in diffraction intensity is reproduced in this case.

The discrepancies between theory and experiment are best understood in terms of limitations in the model used. The above analysis is based on a color center model for photosensitivity and assumes that only changes in the absorption spectrum within the wavelength range investigated (190 to 1600 nm) will contribute to the observed refractive index variation. Clearly, the optical absorption can undergo significant band modification in the wavelength range beyond our measurement capabilities [20]. Such effects were not included in the present analysis. This issue may likely account for the disagreements seen in Figure 14 at lower annealing temperatures. Even with these limitations, however, it is interesting to note that the model does predict a high (>40% of initial value) diffraction intensity at temperatures in excess of 300 C for the LT material. It appears that, while the material has undergone substantial structural rearrangement, the local changes in refractive index serve to maintain the grating contrast.

While the issues mentioned above can also impact the performance of the HT grating model results, the relatively good agreement between the HT data and the modeled behavior in Figure 15, further support the use of a color center model to describe the effect of heat on the performance of a photo-imprinted Bragg grating in these materials.

5. Conclusion

In the present work, we have focused on the thermal stability of photosensitive glasses synthesized using reactive atmosphere, RF-magnetron sputtering and the associated impact on photo-imprinted Bragg gratings within these glasses. Depending upon the substrate temperature used during deposition, different types of photosensitive precursor defects were found that resulted in significant variations in the characteristics of a photo-induced refractive index change.

Optical and magnetic spectroscopy, coupled with isochronal annealing treatments, have revealed that the LT and HT-type glasses also exhibit varied degrees of structural rearrangement at elevated temperatures. In the most extreme case, the LT-type glass showed evidence of short and medium range structural relaxation consistent with the formation of a more interconnected glass network. This structural rearrangement precipitated a transition from oxygen-deficient Ge defect complexes, more characteristic of sputter deposited material, to a population of neutral oxygen vacancies and Ge E' centers that are typically associated with photosensitive effects in conventionally synthesized glass. This modification in the local defect structure also impacts the photosensitive bleaching response of the material and, hence, the dispersion and magnitude of the UV-induced refractive index change.

Differences in the glass structural stability are mirrored by differences in the thermal stability of Bragg gratings that were photo-imprinted into each material. Using a relatively simple approach, based on the validity of the color center model for photosensitivity in these materials and measured changes in intrinsic materials absorption spectrum, thermally mediated modification of Bragg grating performance was simulated.

The model showed qualitative agreement with experimental 1st order diffraction intensity data used to evaluate the state-of-health of gratings photo-imprinted into both LT and HT glass. Indeed, the persistence of the LT-type gratings past the temperature range known to cause changes in the local and medium range atomic structure and an enhancement in the diffracted beam intensity in the HT-type glass were both predicted using the model. While the model did not include all possible mechanisms that could potentially contribute to a refractive index modification in these glasses, these results help to confirm the predominance of a color center-based mechanism for photosensitivity in the sputter-deposited glasses under the optical exposure conditions used.

In past work, we demonstrated that defect engineering dramatically influences the photosensitive properties of germanosilicate glass, allowing the characteristics of the photo-induced refractive index change to be tailored for specific applications. The present research has shown that the manipulation of point defect structure for enhanced optical behavior also significantly influences the environmental stability and reliability of optical devices that are photo-imprinted into these materials. The fundamental dependence of the photosensitive response on the atomic structure of the glass strongly links the environmental stability of the glass structure with the performance of a given photosensitive device. An understanding of these relationships therefore enables the targeted design of optimized photosensitive materials and the development of predictive capabilities useful to insure reliable, stable operation.

Acknowledgement:

Sandia National Laboratories is a multiprogram laboratory operated by Sandia Corporation, a Lockheed Martin Company. This work was supported by the U.S. DOE under contract DE-AC04-94AL85000.

References:

1. P.J. Lemaire, R.M. Atkins V. Mizrahi, and W.A. Reed, Elec. Lett. 29 (1993) 1191.
2. T. Erdogan, V. Mizrahi, P.J. Lemaire, and D. Monroe, J. Appl. Phys. 76 (1994) 73.
3. B.G. Potter, Jr. and K. Simmons-Potter, Nuc. Inst. Meth. in Phys. Res. (NIM B), in press.
4. K. Simmons-Potter, B.G. Potter, Jr., D.C. McIntyre, P.D. Grandon, Appl. Phys. Lett. 68 (1996) 2011.
5. W.L. Warren, K. Simmons-Potter, B.G. Potter, Jr. and J.A. Ruffner, Appl. Phys. Lett. 69 (1996) 1453.
6. B.G. Potter, Jr., K. Simmons-Potter, W.L. Warren, J.A. Ruffner, and D.C. Meister, SPIE 2998 (1997) 146.
7. K. Simmons-Potter, B.G. Potter, Jr. and M. Sinclair, Jpn. J. Appl. Phys. Suppl. 37-1 (1998) 8.
8. K. Simmons-Potter, B.G. Potter, Jr., and W.L. Warren, SPIE 2998 (1997) 93.
9. H. Hosono, Y. Abe, D.L. Kinser, R.A. Weeks, K. Muta, and K. Kawazoe, Phys. Rev. B 46 (1992) 11 445.
10. J. Nishii, K. Fukumi, H. Yamanaka, K. Kawamura, H. Hosono, and H. Kawazoe, Phys. Rev. B 52 (1995) 1661.
11. V. Garino-Canina, Compt. Rend. 242 (1956) 1982.
12. E.J. Friebele and D. L. Griscom, Mater. Res. Soc. Symp. Proc. 61 (1986) 319.
13. H. Verweij, J. Noncryst. Solids 33 (1979) 41.
14. S.K. Sharma, D.W. Matson, J.A. Philpotts, and T.L. Roush, J. Non-Cryst. Solids 68 (1984) 99.
15. B.G. Potter, Jr., R. Ochoa, D.G. Chen, and J.H. Simmons, Opt. Lett. 17 (1992) 1349.
16. K.D. Simmons, G.I. Stegeman, B.G. Potter, Jr., and J.H. Simmons, J. Non-Cryst. Solids 179 (1994) 254.
17. V.B. Neustruev, E.M. Dianov, V.M. Kim, V.M. Mashinskii, M.V. Romanov, A.N. Gur'yanov, V.F. Khopin and V.A. Tikhomirov, Fibers Integr.Opt. 8 (1989) 143.
18. R.J. Hemley, H.K. Mao, P.M. Bell, and B.O. Mysen, Phys. Rev. Lett. 57 (1986) 747.
19. D.J. Durben and G.H. Wolf, Phys. Rev. B 43 (1991) 2355.
20. L.B. Allard, J. Albert, J.L. Brebner, and G.R. Atkins, Opt. Lett. 22 (1997) 819.

Figure Captions:

Figure 1: Representative optical absorption spectra obtained from LT (a) and HT (b) films both in the as-deposited condition and after KrF (248 nm) excimer laser exposure that fully saturated the absorption change in the material (total fluence = 15 kJ/cm^2).

Figure 2: Isochronal annealing effects on the optical absorption spectra collected from LT (a) and HT (b) films previously exposed to a total KrF laser fluence of 15 kJ/cm2. Spectra are shown after several isochronal annealing steps. (15 minutes hold time at each temperature under flowing He).

Figure 3: Isochronal annealing effects on the optical absorbance at 200 and 240 nm for LT material starting in the as-deposited state (a) and after an initial UV exposure (b) to saturate the absorption change. The material in (b) was subjected to a second UV exposure, followed by another isochronal anneal sequence. (15 minutes hold time at each temperature under flowing He).

Figure 4: Isochronal annealing effects on the optical absorbance at 200 and 240 nm for HT material starting in the as-deposited state (a) and after an initial UV exposure (b) to saturate the absorption change. (15 minutes hold time at each temperature under flowing He).

Figure 5: Representative optical absorption spectra collected from an LT film illustrating the modification in UV-induced absorption change observed after isochronal annealing.

Corresponding EPR spin densities measured from the sample are given the inset table. Axes are shifted for the as-deposited film (left vertical axis) and the annealed data (right vertical axis, for clarity).

Figure 6: Unpolarized waveguide Raman spectra for LT and HT films collected from as-deposited material and after an anneal at 465 C for 30 minutes in flowing He.

Figure 7: Representative EPR spectra showing the effect of UV-exposure (fluence = 15 kJ/cm2) in an LT film.

Figure 8: Representative EPR spectra showing the effect of UV-exposure (fluence = 15 kJ/cm2) in an HT film.

Figure 9: EPR Ge unpaired spin density plotted as a function of the isochronal annealing temperature for both as-deposited (a) and UV-exposed (b) LT material. The material in (b) was subjected to a second UV exposure, followed by another isochronal anneal sequence. The estimated noise level for the EPR measurement is indicated on the graphs. Data points falling below this level are provided for indication only and were obtained from raw data reduction consistent with the procedure discussed in the Experimental section and that used for all other data points in the plots.

Figure 10: EPR Ge E' spin density plotted as a function of the isochronal annealing temperature for both as-deposited and UV-exposed HT material. The estimated noise

level for the EPR measurement is indicated on the graph. Data points falling below this level are provided for indication only and were obtained from raw data reduction consistent with the procedure discussed in the Experimental section and that used for all other data points in the plot.

Figure 11: Representative EPR spectrum obtained from a previously UV-irradiated and annealed LT film (bottom). The effect of a second UV-exposure is observed in the upper spectrum.

Figure 12: Normalized, first-order, diffracted intensity from a photosensitive Bragg grating structure imprinted in both LT and HT materials plotted with isochronal annealing temperature. (15 minutes hold time at each temperature under flowing He).

Figure 13: Schematic showing hypothetical index profile for a photo-imprinted Bragg grating structure. The graph depicts the profile anticipated for an LT-type material, i.e. the UV-exposed regions exhibit a lower refractive index.

Figure 14: Modeled vs. experimentally observed normalized, first-order, diffracted intensities for photo-imprinted Bragg gratings in an LT film.

Figure 15: Modeled vs. experimentally observed normalized, first-order, diffracted intensities for photo-imprinted Bragg gratings in an HT film.

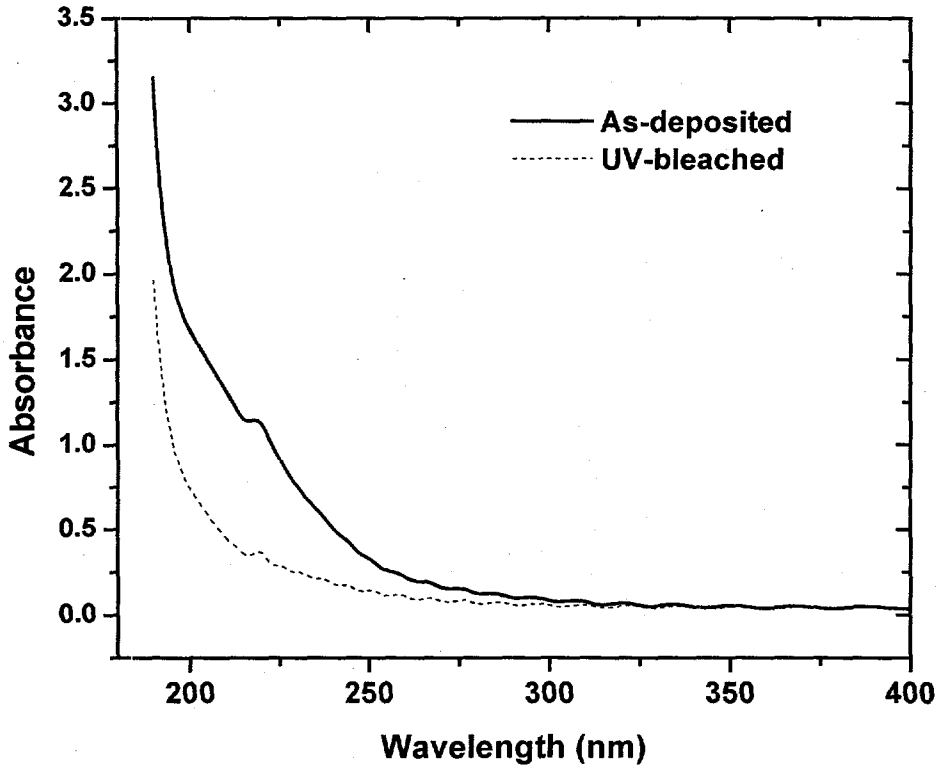
3.5
3.0
2.5
2.0
1.5
1.0
0.5
0.0
Absorbance
As-deposited
UV-bleached
200
250
300
350
400
Wavelength (nm)

Figure 1a

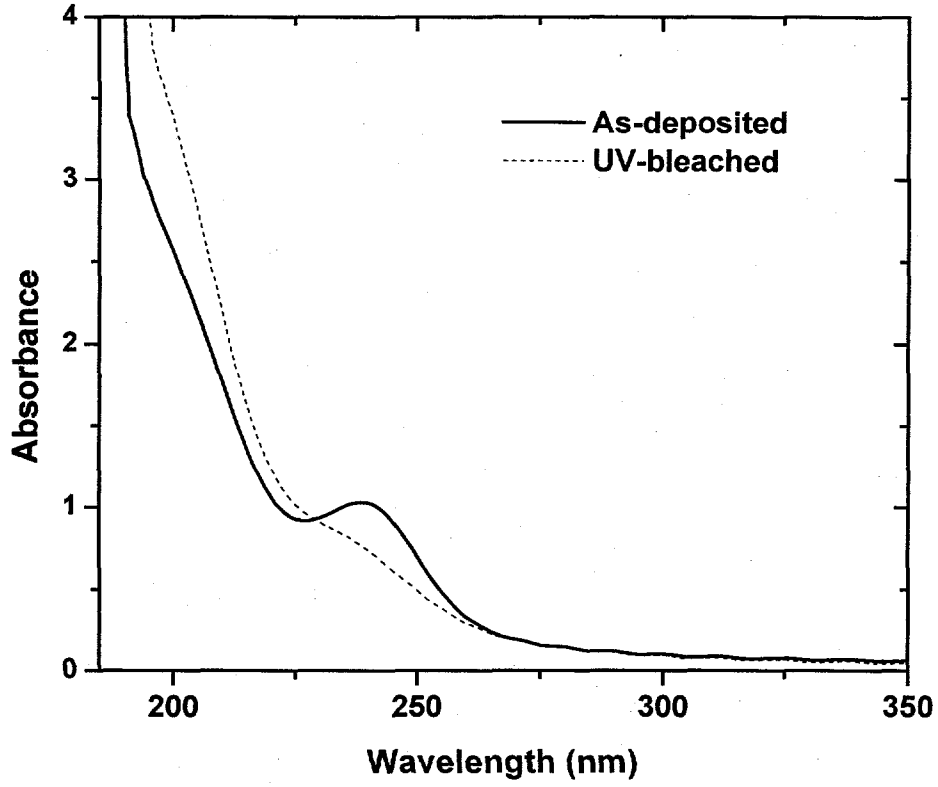
As-deposited
UV-bleached
Absorbance
Wavelength (nm)
0
1
2
3
4
200
250
300
350

Figure 1b

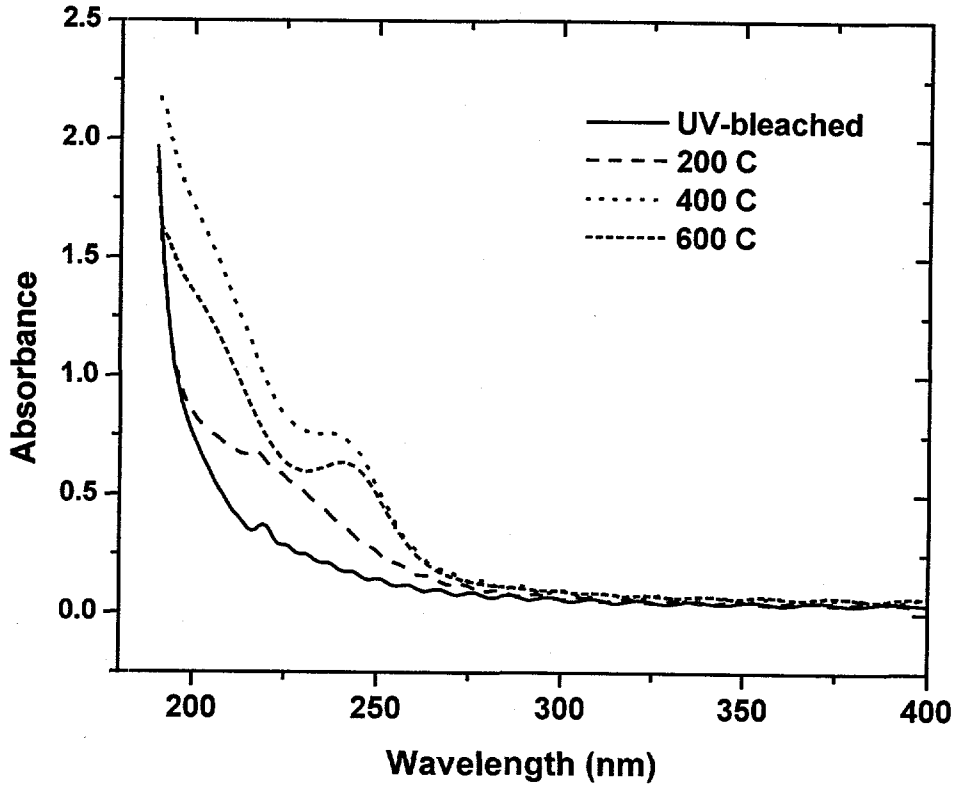
2.5
2.0
1.5
1.0
0.5
0.0
Absorbance
200
250
300
350
400
Wavelength (nm)
UV-bleached
200 C
400 C
600 C

Figure 2a

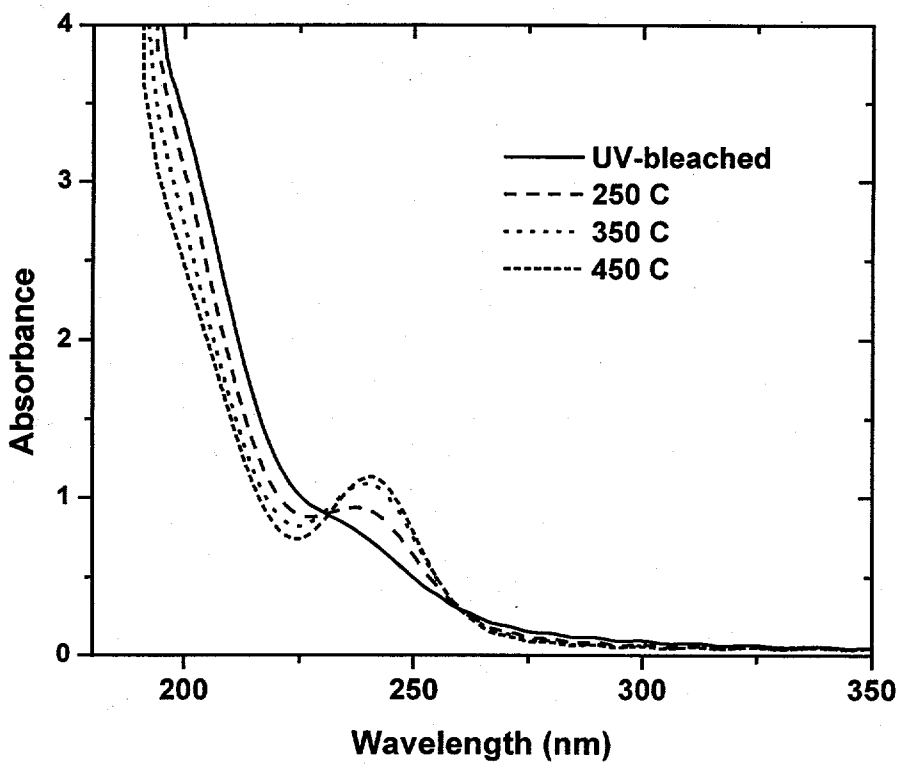
Absorbance
Wavelength (nm)
UV-bleached
250 C
350 C
450 C
0
1
2
3
4
200
250
300
350

Figure 2b

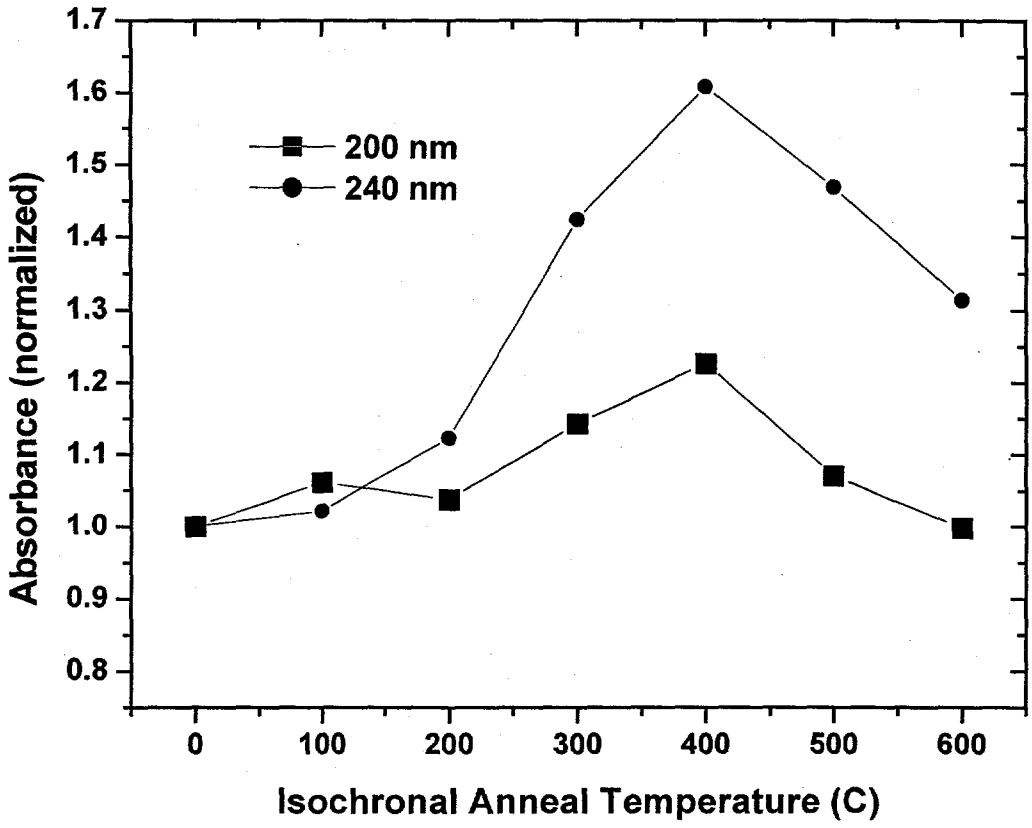
1.7
1.6
1.5
1.4
1.3
1.2
1.1
1.0
0.9
0.8
Absorbance (normalized)
200 nm
240 nm
0
100
200
300
400
500
600
Isochronal Anneal Temperature (C)

Figure 3a:

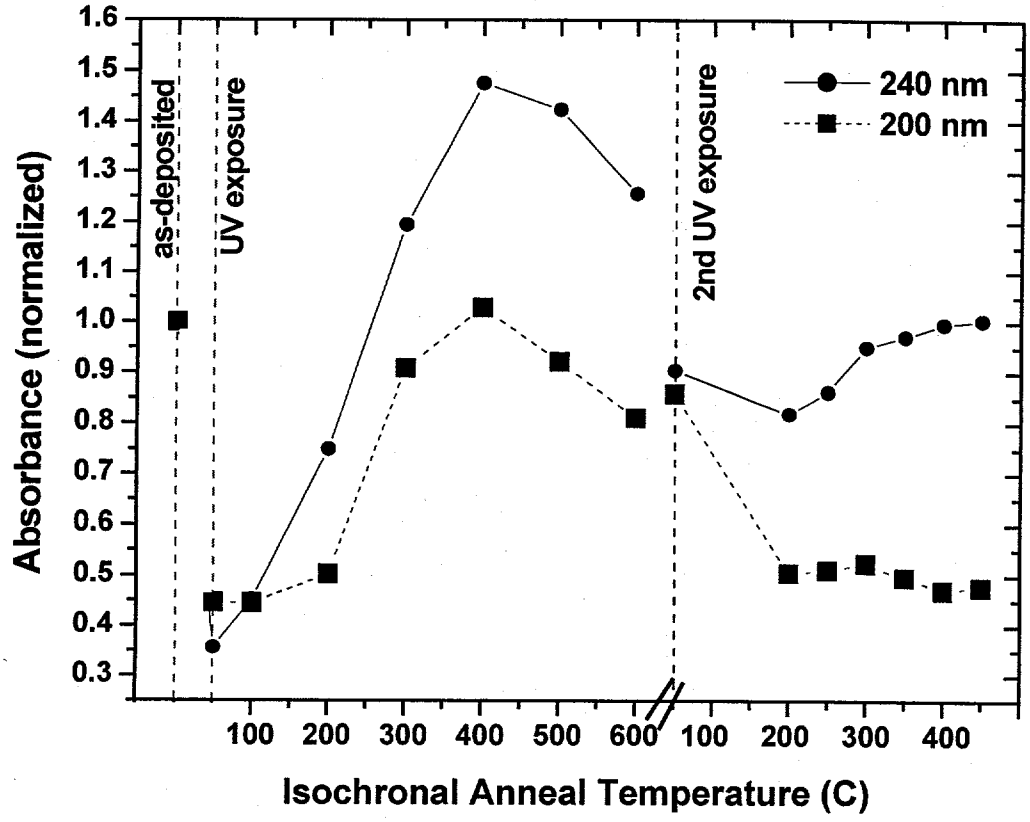
Absorbance (normalized)
Isochronal Anneal Temperature (C)
as-deposited
UV exposure
2nd UV exposure
240 nm
200 nm
1.6
1.5
1.4
1.3
1.2
1.1
1.0
0.9
0.8
0.7
0.6
0.5
0.4
0.3
100
200
300
400
500
600
100
200
300
400

Figure 3b:

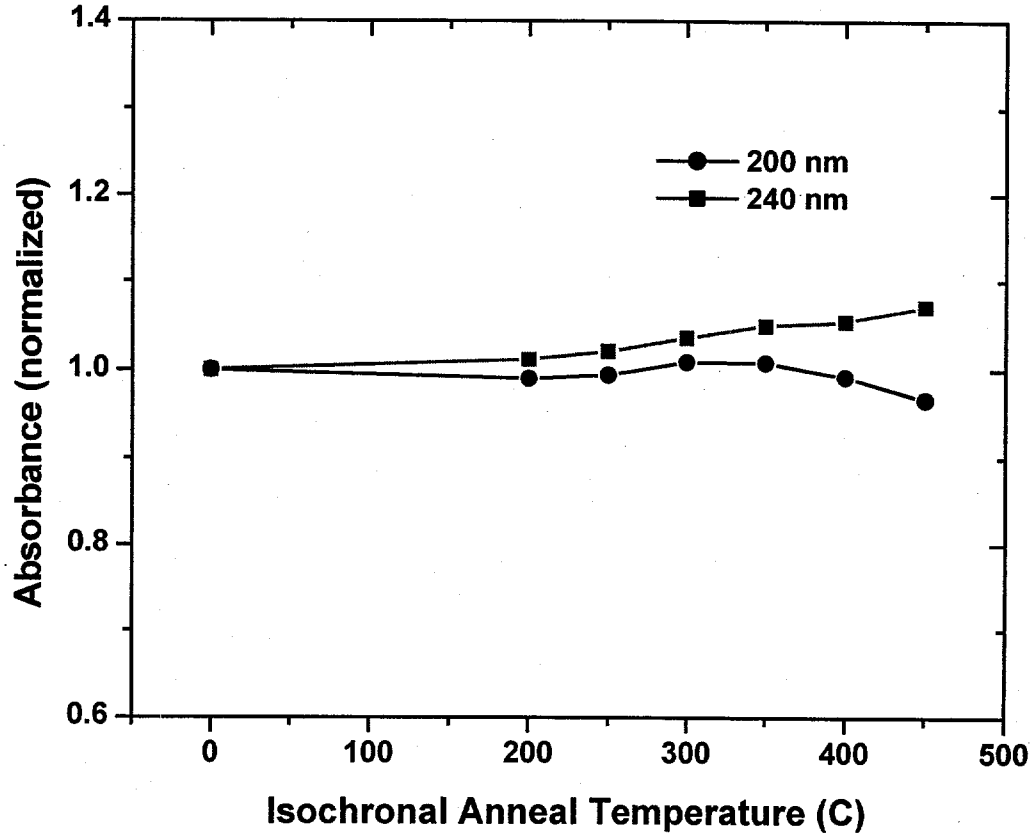
1.4
1.2
1.0
0.8
0.6
Absorbance (normalized)
200 nm
240 nm
0
100
200
300
400
500
Isochronal Anneal Temperature (C)

Figure 4a:

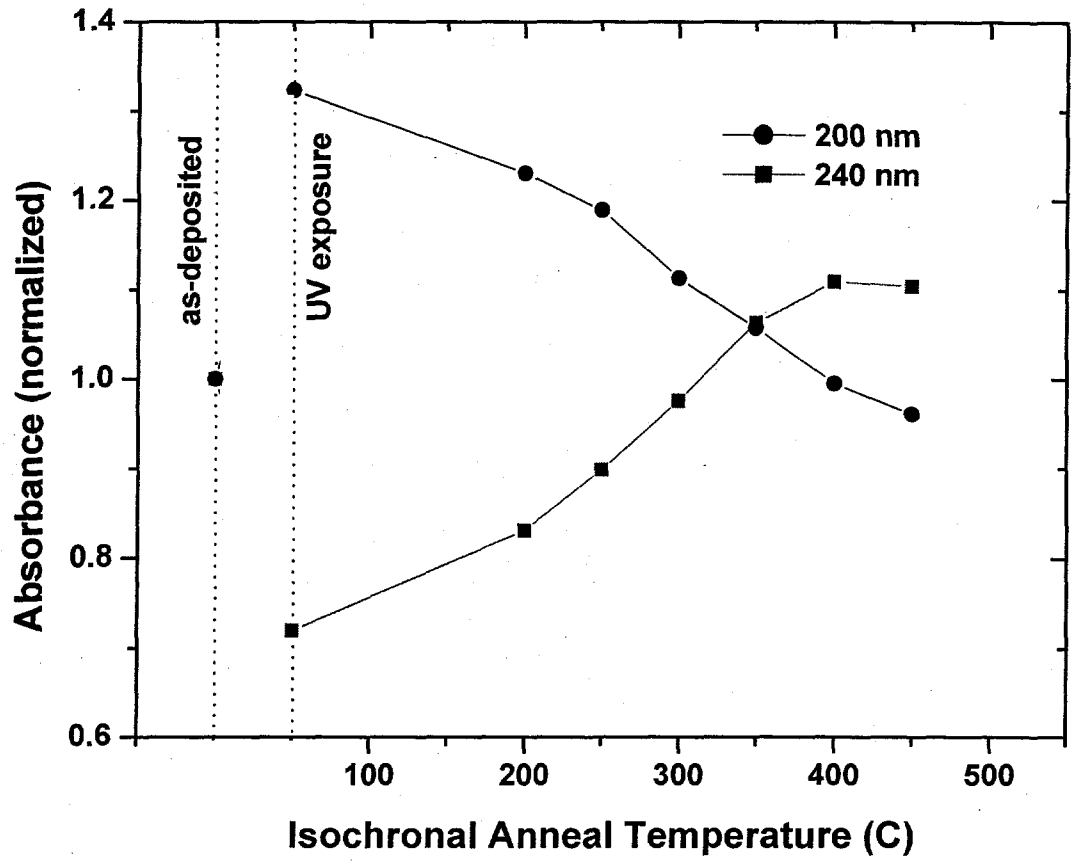
1.4
1.2
1.0
0.8
0.6
Absorbance (normalized)
as-deposited
UV exposure
200 nm
240 nm
100
200
300
400
500
Isochronal Anneal Temperature (C)

Figure 4b.

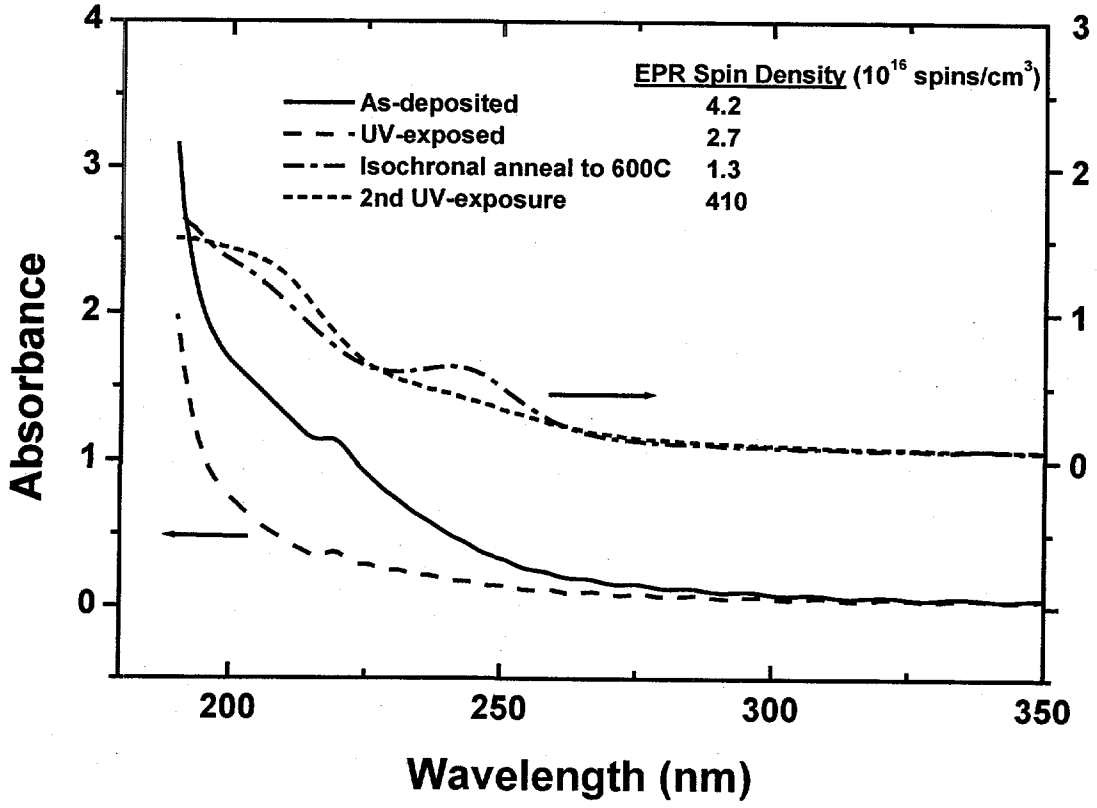
EPR Spin Density (10^{16} spins/cm^3)
As-deposited 4.2
UV-exposed 2.7
Isochronal anneal to 600C 1.3
2nd UV-exposure 410
Absorbance
Wavelength (nm)
4
3
2
1
0
200
250
300
350

Figure 5.

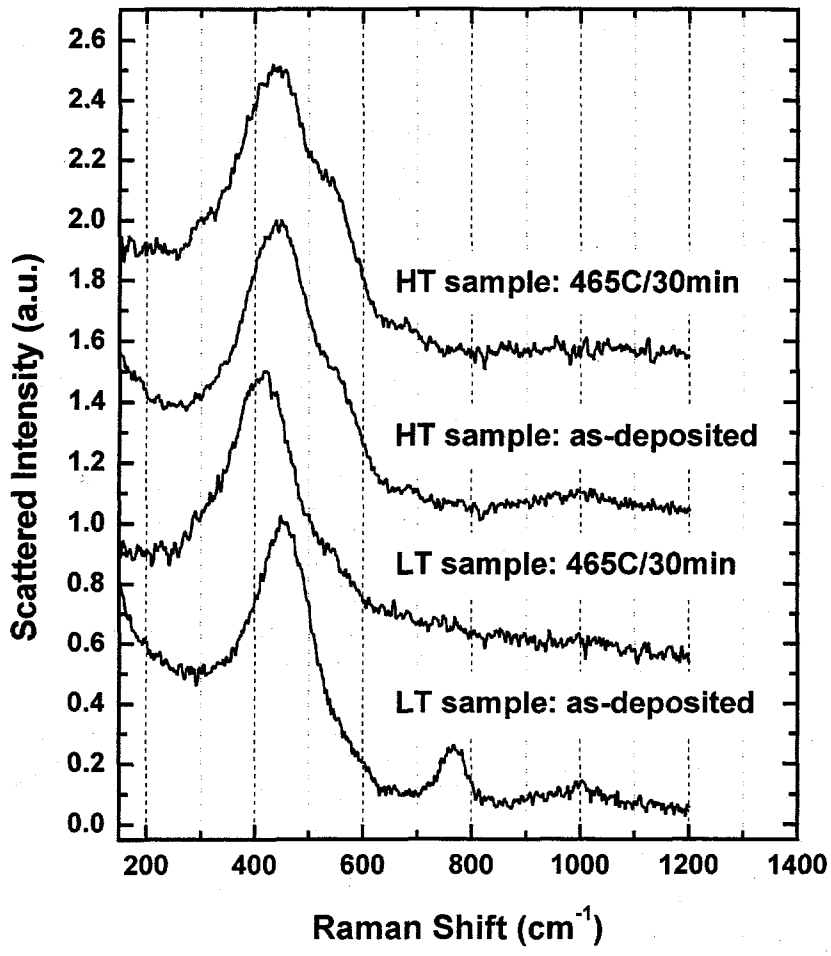
Scattered Intensity (a.u.)
Raman Shift (cm^{-1})
HT sample: 465C/30min
HT sample: as-deposited
LT sample: 465C/30min
LT sample: as-deposited
0.0
0.2
0.4
0.6
0.8
1.0
1.2
1.4
1.6
1.8
2.0
2.2
2.4
2.6
200
400
600
800
1000
1200
1400

Figure 6.

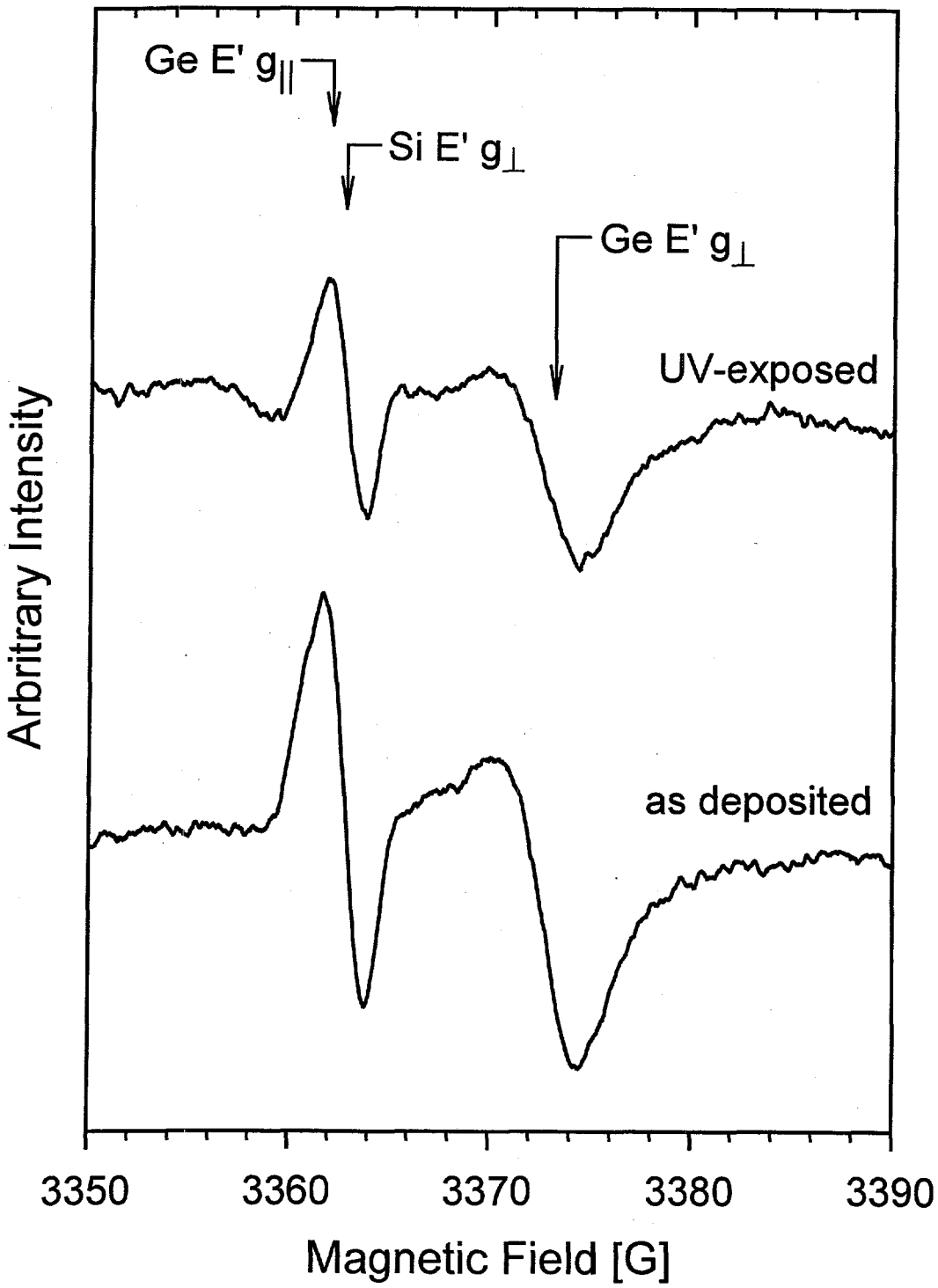
Ge E' g||
Si E' g⊥
Ge E' g⊥
UV-exposed
as deposited
Arbitrary Intensity
3350
3360
3370
3380
3390
Magnetic Field [G]

Figure 7:

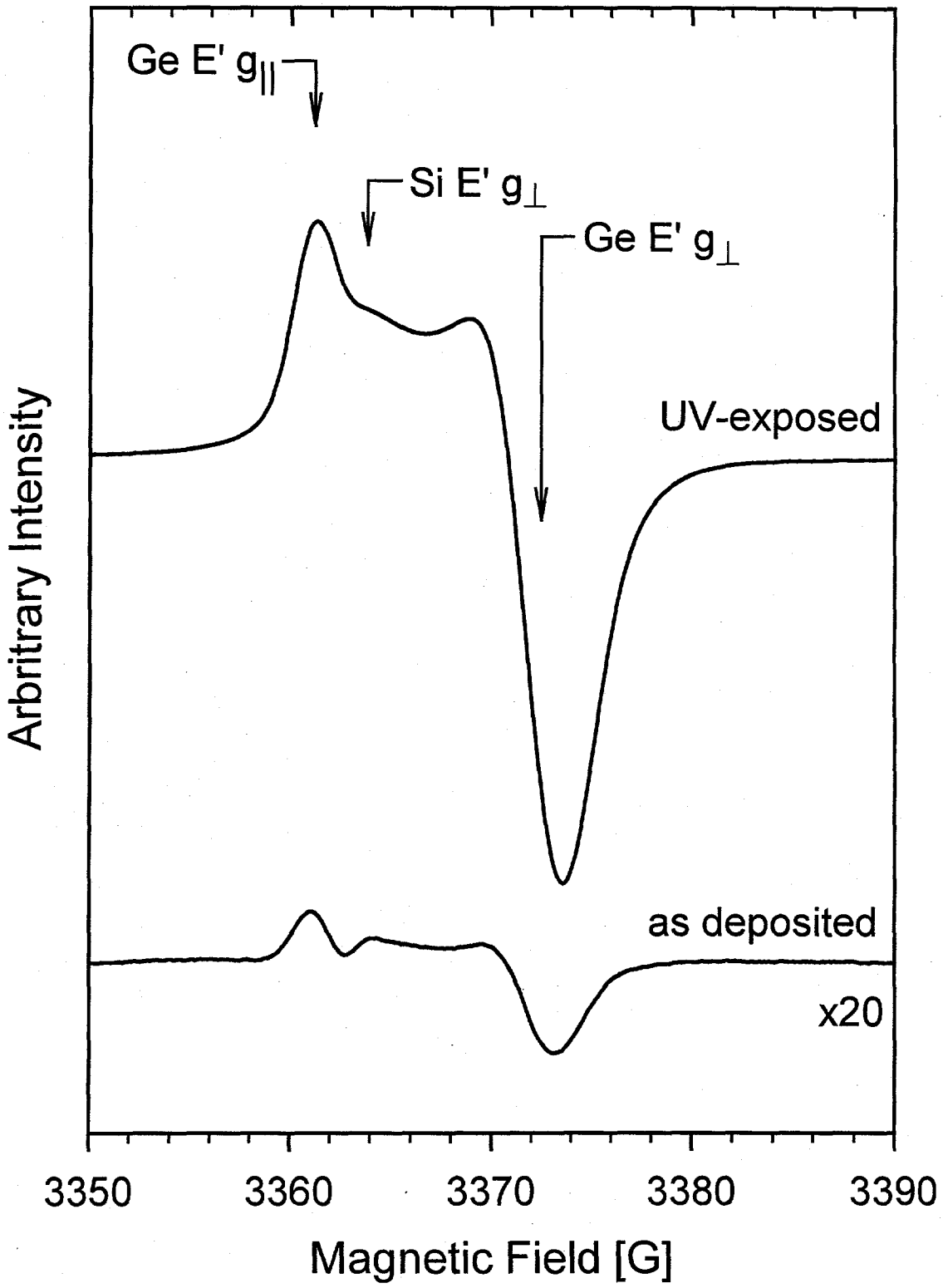
Ge E' g||
Si E' g⊥
Ge E' g⊥
UV-exposed
as deposited
x20
Arbitrary Intensity
3350
3360
3370
3380
3390
Magnetic Field [G]

Figure 8:

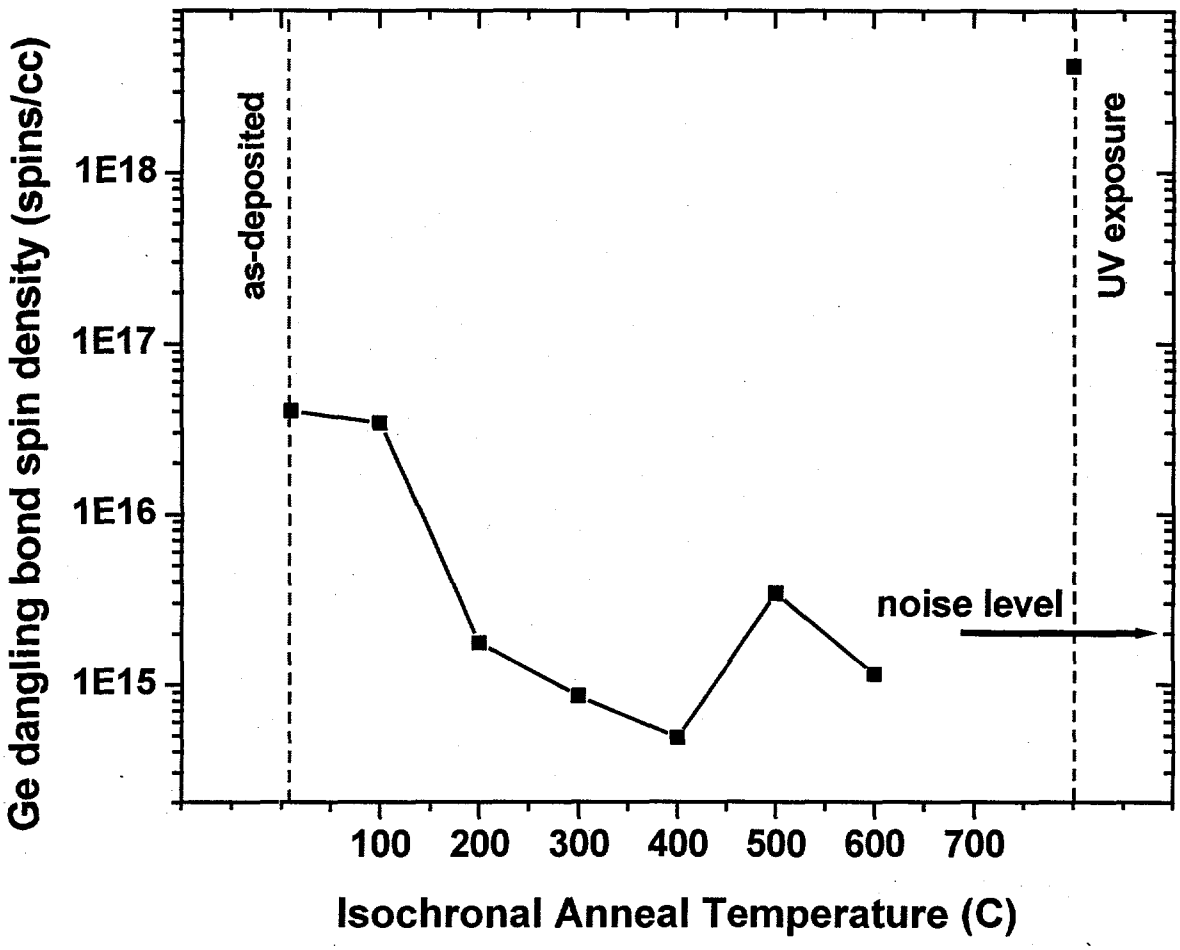
Ge dangling bond spin density (spins/cc)
1E18
1E17
1E16
1E15
as-deposited
UV exposure
noise level
100
200
300
400
500
600
700
Isochronal Anneal Temperature (C)

Figure 9a:

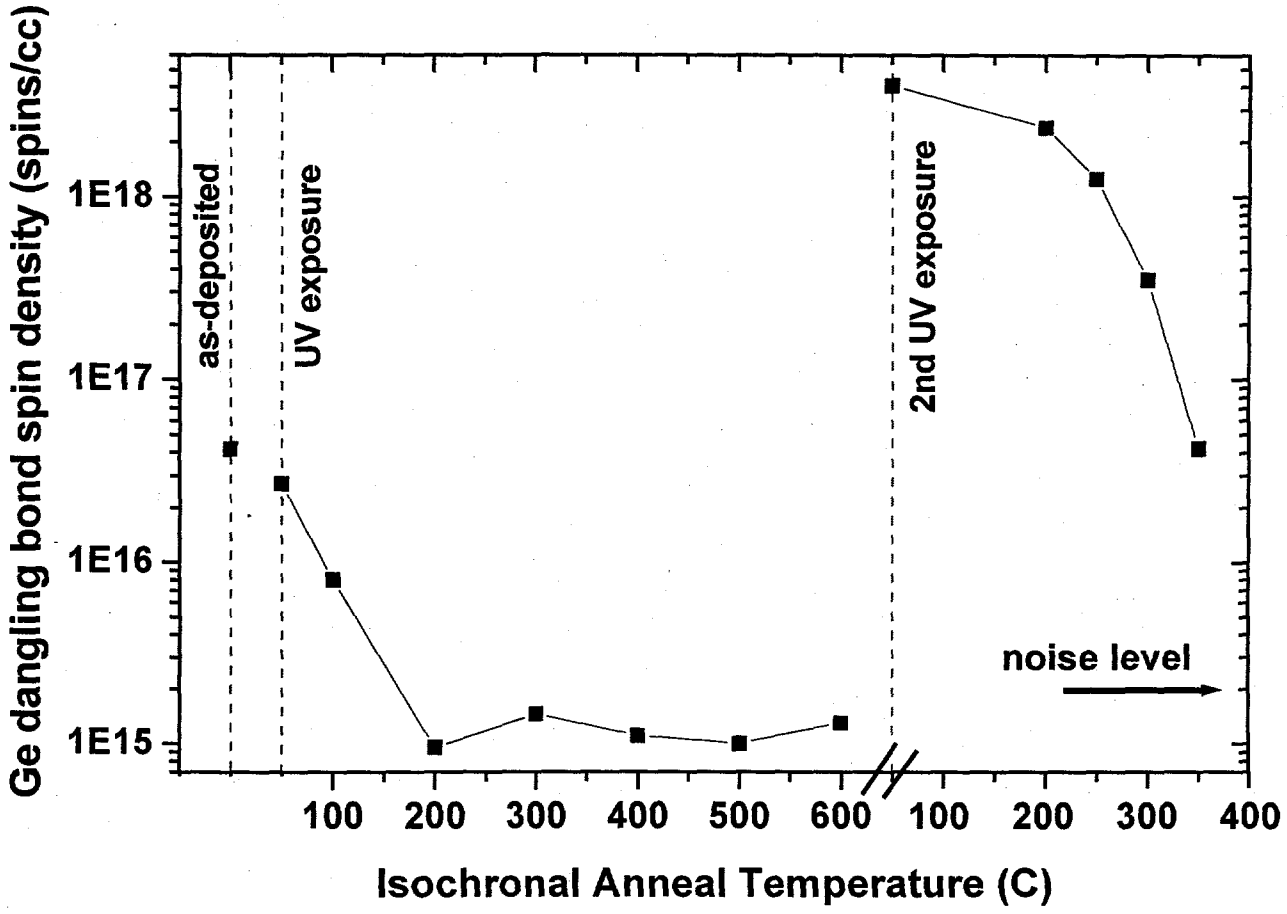
Ge dangling bond spin density (spins/cc)
1E18
1E17
1E16
1E15
as-deposited
UV exposure
2nd UV exposure
noise level
100
200
300
400
500
600
100
200
300
400
Isochronal Anneal Temperature (C)

Figure 9b:

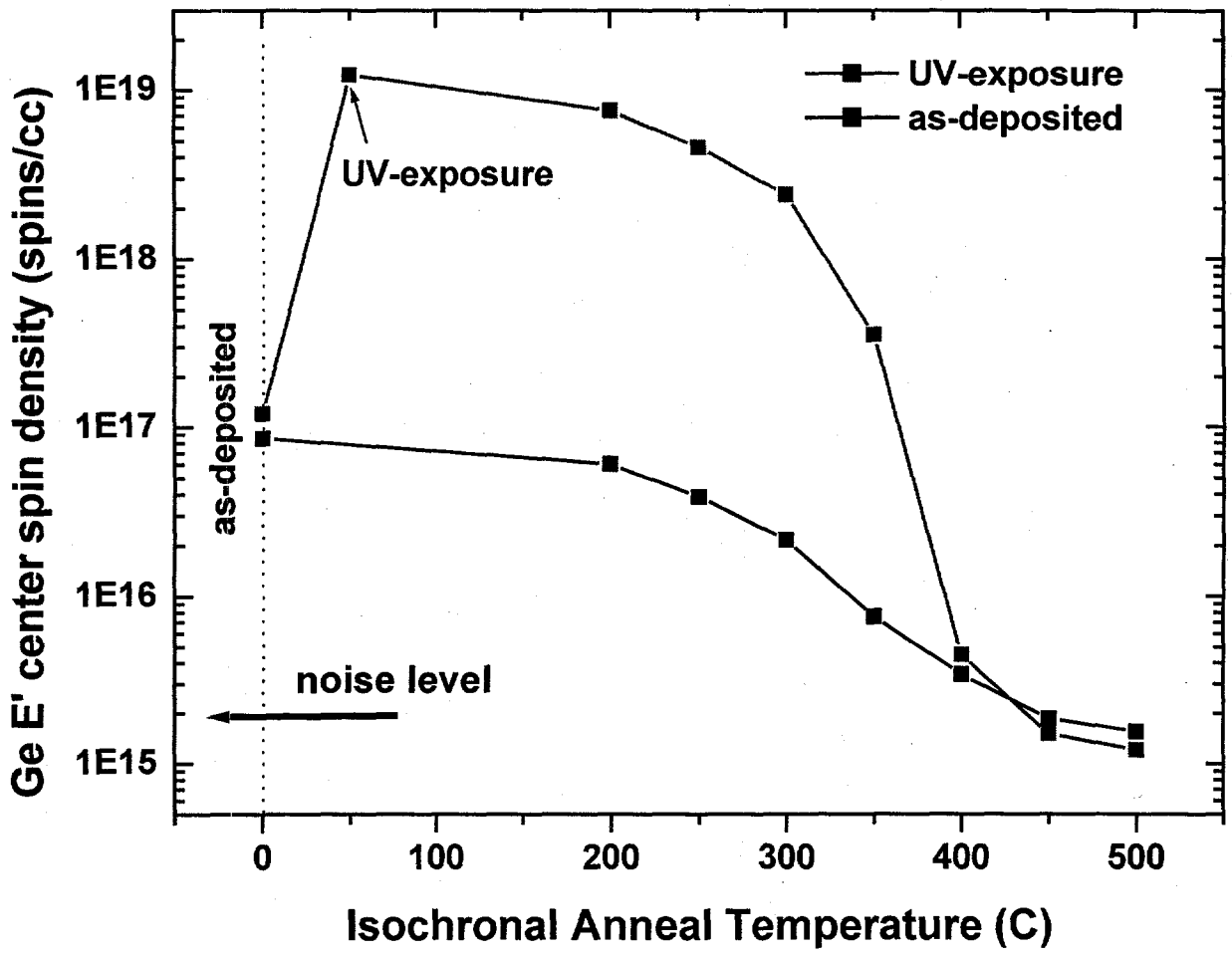
Ge E' center spin density (spins/cc)
1E19
1E18
1E17
1E16
1E15
0
100
200
300
400
500
Isochronal Anneal Temperature (C)
UV-exposure
as-deposited
UV-exposure
as-deposited
noise level

Figure 10:

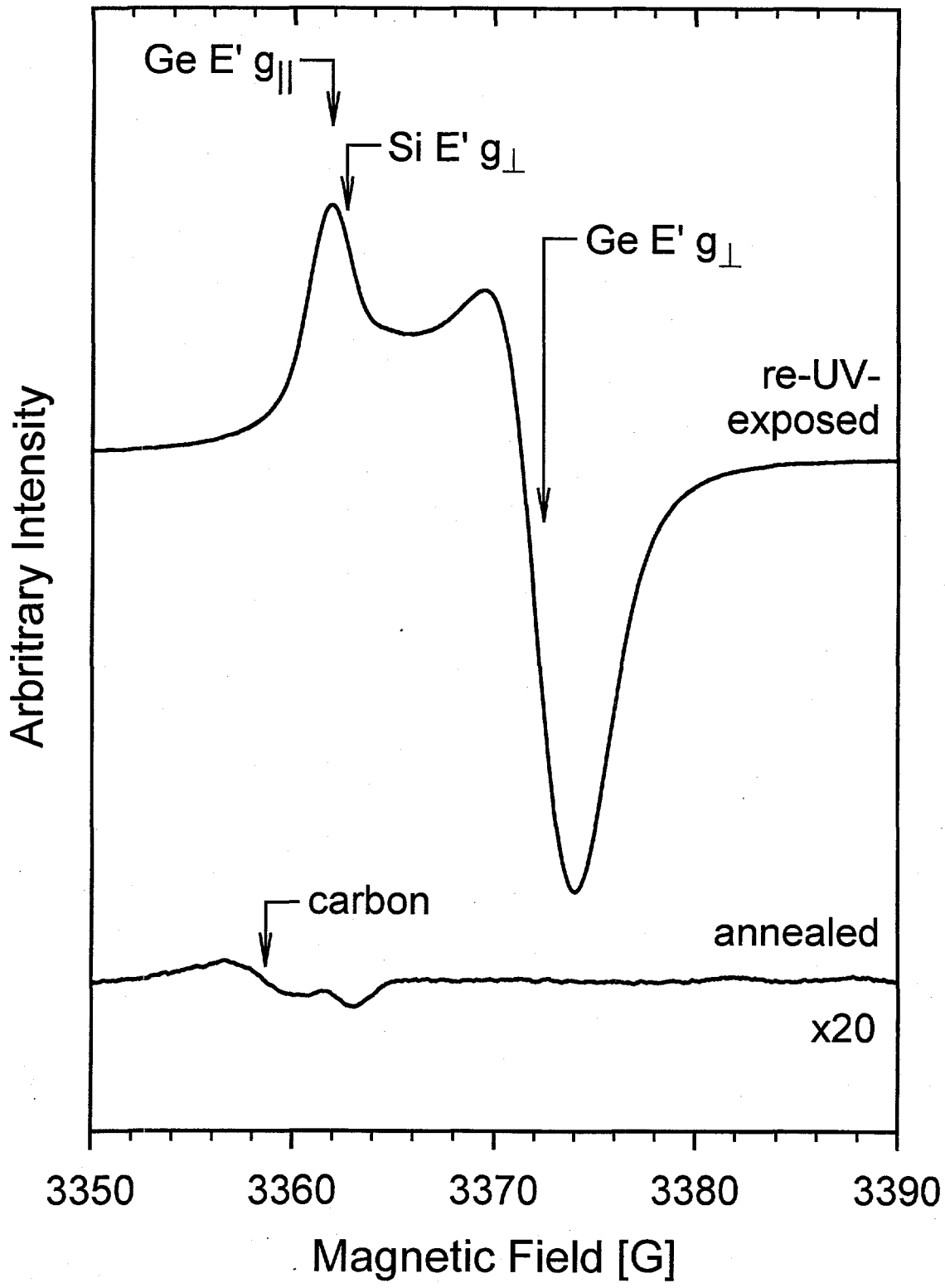
Ge E' g||
Si E' g⊥
Ge E' g⊥
re-UV-
exposed
carbon
annealed
x20
Arbitrary Intensity
3350
3360
3370
3380
3390
Magnetic Field [G]

Figure 11:

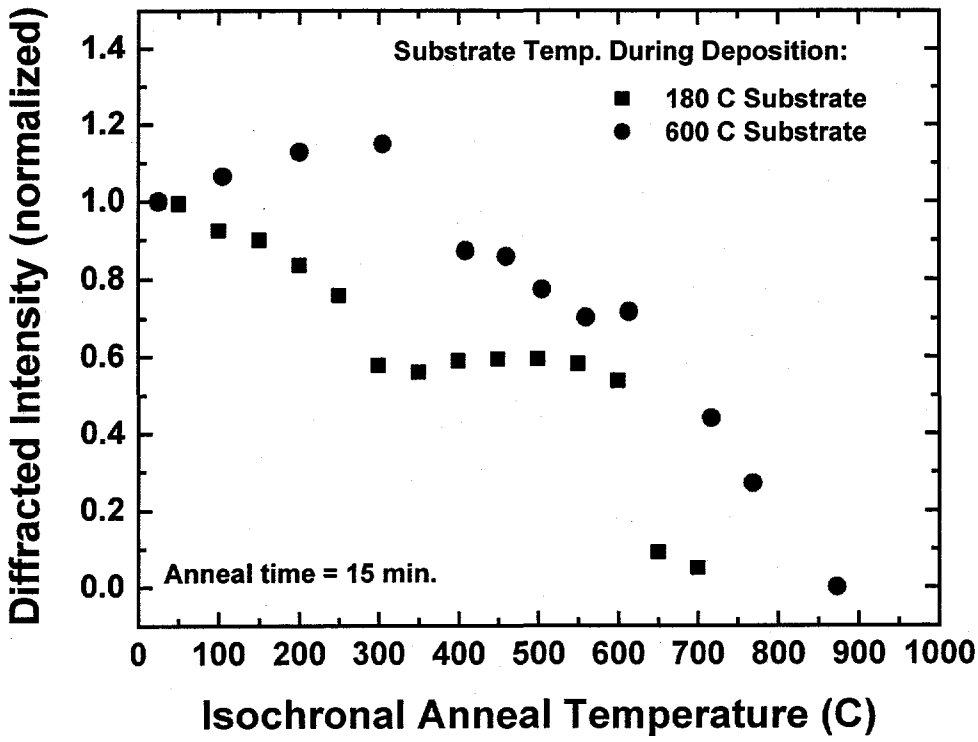
Substrate Temp. During Deposition:
180 C Substrate
600 C Substrate
Anneal time = 15 min.
Diffracted Intensity (normalized)
Isochronal Anneal Temperature (C)
0.0
0.2
0.4
0.6
0.8
1.0
1.2
1.4
0
100
200
300
400
500
600
700
800
900
1000

Figure 12

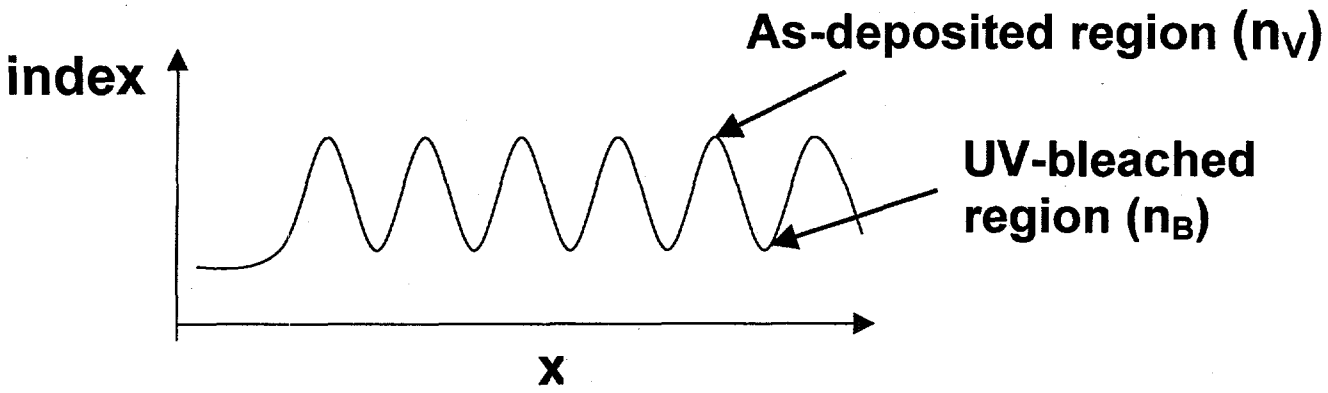

Grating Contrast, $C = n_B - n_V$

Figure 13

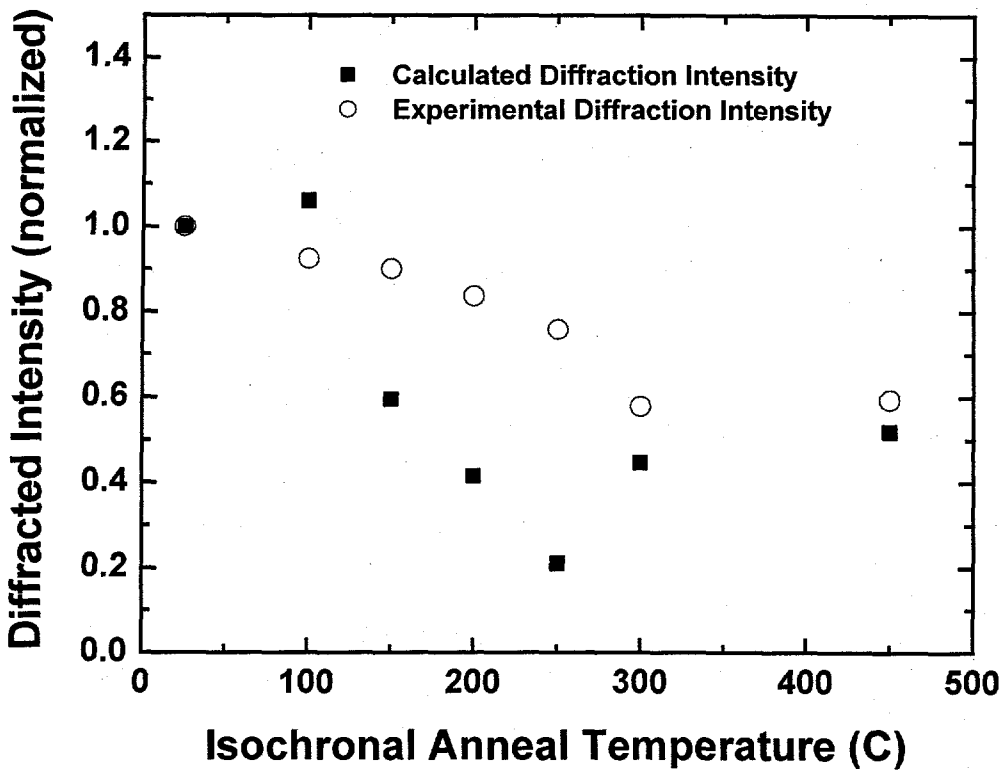
Diffracted Intensity (normalized)
1.4
1.2
1.0
0.8
0.6
0.4
0.2
0.0
0
100
200
300
400
500
Isochronal Anneal Temperature (C)
Calculated Diffraction Intensity
Experimental Diffraction Intensity

Figure 14:

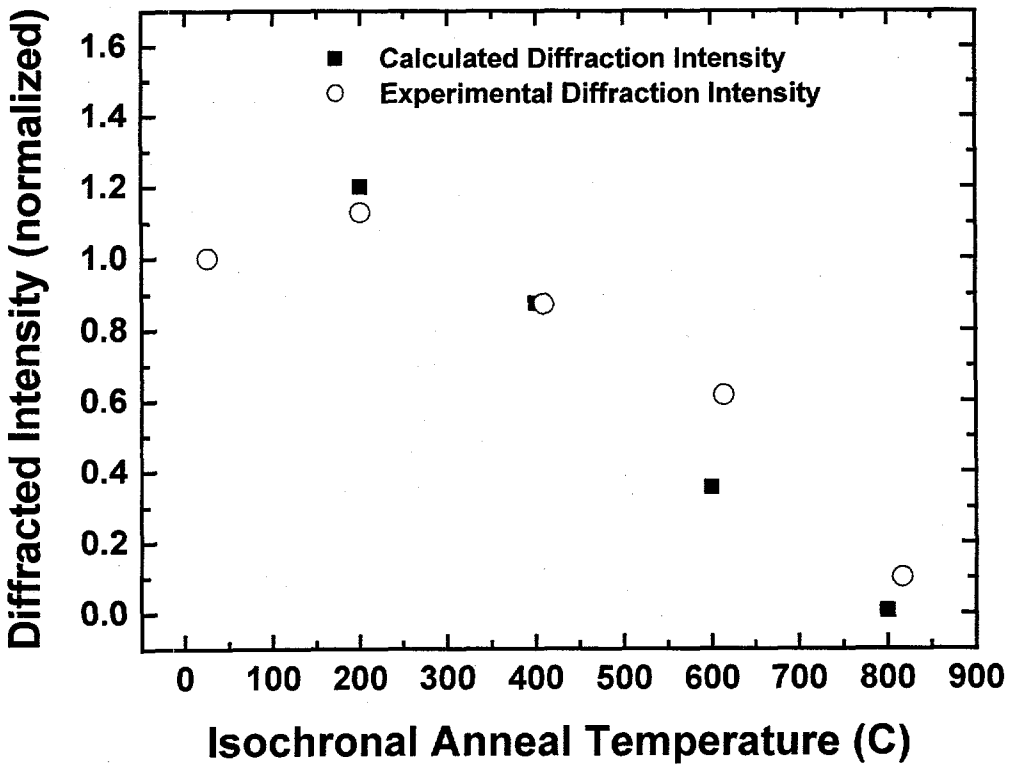
Calculated Diffraction Intensity
Experimental Diffraction Intensity
Diffracted Intensity (normalized)
1.6
1.4
1.2
1.0
0.8
0.6
0.4
0.2
0.0
0
100
200
300
400
500
600
700
800
900
Isochronal Anneal Temperature (C)

Figure 15: